Scheduling Framework Using Dynamic Optimal Power Flow for Battery Energy Storage Systems

Fulin Fan, Ivana Kockar, *Senior Member*, *IEEE*, Han Xu, and Jingsi Li

***Abstract*—Battery energy storage systems (BESS) are instrumental in the transition to a low carbon electrical network with enhanced flexibility, however, the set objective can be accomplished only through suitable scheduling of their operation. This paper develops a dynamic optimal power flow (DOPF)-based scheduling framework to optimize the day(s)-ahead operation of a grid-scale BESS aiming to mitigate the predicted limits on the renewable energy generation as well as smooth out the network demand to be supplied by conventional generators. In DOPF, all the generating units, including the ones that model the exports and imports of the BESS, across the entire network and the complete time horizon are integrated on to a single network. Subsequently, an AC-OPF is applied to dispatch their power outputs to minimize the total generation cost, while satisfying the power balance equations, and handling the unit and network constraints at each time step coupled with inter-temporal constraints associated with the state of charge (SOC). Furthermore, the DOPF developed here entails the frequently applied constant current-constant voltage charging profile, which is represented in the SOC domain. Considering the practical application of a 1 MW BESS on a particular 33 kV network, the scheduling framework is designed to meet the pragmatic requirements of the optimum utilization of the available energy capacity of BESS in each cycle, while completing up to one cycle per day.**

***Index Terms*—Battery energy storage, day(s)-ahead scheduling, dynamic optimal power flow, load smoothing, renewable energy.**

I. Introduction

As a means to render grid support, energy storage finds widespread application both in distribution and transmission networks not only to impart reinforced flexibility to the electrical grids, but also to facilitate the transition of the grids to low carbon energy systems with greater decentralization [1]. Depending on the location in the grid, energy storage systems (ESS) can offer potential benefits, such as enabling the integration of renewables [2], smoothing the demand [3], providing ancillary services [4], and curtailing the demand for network reinforcement [5], [6]. In the last decade, the acceleration in the development of battery technology and the dramatic decline in battery prices [7] boosted the technical and economic feasibility in terms of the battery ESS (BESS) implementation in the power systems.

Known to provide longer storage durations and fewer cycles per day, grid-scale BESS are typically applied to the time shift of renewable and conventional generation [8], [9], thereby enhancing the operational efficiency of the generating units together with curbing the utilization of fossil fuels. The functioning of BESS, i.e., the time and rate at which the BESS imports or exports, can either be determined in real time or be planned several hours or days ahead. Regulated by real-time algorithms, BESS can instantaneously respond to the frequency deviation [4] and smooth out the fluctuation occurring in the renewable generator (RG) export [10]–[12] or system demand [3]. Although the real-time control evades the problem caused by forecast errors, it predominantly concentrates on the RG curtailment or load level at the present instant only, and is likely to fully charge the BESS or consume all the stored energy even before reaching a particular time period in the future when the BESS operation would be required to further smooth out the system demand and generator export.

Majority of the research related to BESS operation planning deals with the day(s)-ahead schedules, which are driven by different objectives, including but not limited to a minimized cost (or a maximized revenue) of a BESS integrated system [13]–[15] and an optimized utilization of renewable generation [16], [17]. In addition to electricity generation costs, BESS-related adaptive operation and distribution networking costs are reviewed in [13] and [14], respectively, to formulate an economic scheduling of the BESS as well as the associated power plants. In [15], day-ahead schedules of a BESS are deliberated to maximize the revenues from the energy arbitrage based on the predicted electricity prices of day-ahead markets. For the BESS co-located with RGs, their schedules could be optimized either to mitigate the predicted RG curtailment [16], [17] or to amend the output dispatch plans of RGs in the interest of energy arbitrage [18]. For quite some time now, optimal power flow (OPF) [19] has served as an effective tool to optimally dispatch generating units in a power system at a particular instant by minimizing a selected objective function. For addressing the scheduling problem across multiple time steps, multi-period or dynamic OPF (DOPF) is proposed to formulate the inter-temporal characteristics of BESS and optimize day(s)-ahead plans under a particular scheduling objective (e.g., minimizing the total generation cost), while sat-

Manuscript received July 31, 2020; revised December 30, 2020; accepted March 18, 2021. Date of online publication December 30, 2021; date of current version January 5, 2022.

F. L. Fan (ORCID: https://orcid.org/0000-0003-2450-6877) and I. Kockar (corresponding author, e-mail: ivana.kockar@strath.ac.uk) are with the Department of Electronic and Electrical Engineering, University of Strathclyde, Glasgow, G1 1XW, U.K.

H. Xu is with the Power Networks Demonstration Centre, Glasgow, G68 0EF, U.K.

J. S. Li is with the Department of Civil and Environmental Engineering, University of Strathclyde, Glasgow, G1 1XJ, U.K.

DOI: 10.17775/CSEEJPES.2020.03710

isfying the power balance and handling operating constraints in spatiotemporal horizons [17]. In [20] and [21], DOPF is further improved to deal with the prediction uncertainties of system demands and/or available power of the RGs.

Although published scheduling methods have effectively exhibited their capability of optimally planning BESS cycles, the majority of them assume that a BESS can always import at its rated power, while disregarding the fact that the charging phase is generally regulated in accordance to a specific pragmatic profile, such as the prevalent constant current (CC)-constant voltage (CV) method [22]. The reason could be because the CC-CV profile presumes that a battery imports constantly at the maximum allowable rates $|\underline{P}_{\text{ch}}|$ specified in time domain, which appears impractical in the scheduling of a grid-scale BESS where the import is determined by the RG curtailment and/or demand troughs. To address this issue, this paper converts the CC-CV profile $|\underline{P}_{\text{ch}}|$ from the time domain to the state of charge (SOC) domain, and then integrates the SOC-dependent $|\underline{P}_{\text{ch}}|$ within the DOPF, which is employed here to optimize the day(s)-ahead schedule of a 1 MW BESS, with the objective of mitigating the predicted limits on RG export and smoothing the demand to be supplied by the conventional generating units on a particular 33 kV network. Furthermore, to fulfil the pragmatic requirements of the optimum utilization of the available energy capacity of BESS in each cycle and execute up to one full cycle per day, this paper devises a scheduling framework that divides a plan time horizon into various charging and discharging periods at each of the potential split time points, and then selects the DOPF-based schedule that results in a complete battery cycle with the minimal overall generation cost.

Herein, the DOPF-based scheduling framework is tested based on the 15-minute average load data of the network over 2 years. Hourly average wind speeds used for synthesizing the available power outputs of wind farms on the network during the same period were provided by the British Atmospheric Data Centre [23].

The paper is structured as follows: Section II presents the DOPF and operational constraints specified for the 33 kV network and BESS; Section III introduces the scheduling framework and the modeling of wind generation inputs; Section IV presents an assessment of the optimized day(s)-ahead schedules in terms of the practical scheduling objectives and requirements; and Section V presents conclusions and recommendations for future work.

II. DOPF WITH OPERATIONAL CONSTRAINTS

A. Dynamic Optimal Power Flow (DOPF)

In an OPF problem, the control and state variables of a power system at a particular time step are determined to minimize a predefined objective function [19], [24]. DOPF extends an OPF problem formulation in the time domain, managing the optimization across the system and the time horizon. In DOPF, the power system under consideration must first satisfy the power balance equations along with the unit and system constraints at each time step within the plan time horizon independently; then the systems at all future time steps are correlated with each other by formulating additional equality and/or inequality constraints related to inter-temporal technologies (e.g., energy storage). The inter-temporal constraint typically formulated in the BESS scheduling problem is based on the state of charge (SOC) of the BESS, which is calculated by its imports and exports and must be maintained within a specified range [17], [20].

Given a plan time horizon consisting of T consecutive time steps, a simplified network at each future time step t ($t = 1, \cdots, T$) is shown in Fig. 1, where terms $\theta^{(t-1)n_{\text{b}}+j}$ and $V^{(t-1)n_{\text{b}}+j}$ ($j = 1, \cdots, n_{\text{b}}$) represent the voltage angle and magnitude of the j^{th} bus, respectively; real and reactive powers produced by the i^{th} generator are $P_{\text{g}}^{(t-1)n_{\text{g}}+i}$ and $Q_{\text{g}}^{(t-1)n_{\text{g}}+i}$ ($i = 1, \cdots, n_{\text{g}}$), and those consumed at the j^{th} bus are $P_{\text{d}}^{(t-1)n_{\text{b}}+j}$ and $Q_{\text{d}}^{(t-1)n_{\text{b}}+j}$, respectively; the charge and discharge of BESS are modeled by two virtual generators which produce negative and positive active powers (i.e., P_{ch}^{t} and P_{dis}^{t}), respectively, at a particular time step t. Subsequently, the networks across T time steps correlated by the SOC can be deemed as a single virtual network for the purpose of DOPF implementation.

Herein, the DOPF problem is formulated based on a standard AC-OPF formulation [25]. The vector of optimization variables $X^{\text{T}} = [\theta^{(t-1)n_{\text{b}}+j}, V^{(t-1)n_{\text{b}}+j}, P_{\text{g}}^{(t-1)n_{\text{g}}+i}, Q_{\text{g}}^{(t-1)n_{\text{g}}+i}, P_{\text{ch}}^{t}, P_{\text{dis}}^{t}]$ in the single virtual network is calculated to minimize the overall generation costs across T time steps, based on the cost function $f_{\text{g}}^{i}(\cdot)$ specified for each actual generator:

$$X = \arg\min_{X} \sum_{t=1}^{T} \sum_{i=1}^{n_{\text{g}}} f_{\text{g}}^{i}\left(P_{\text{g}}^{(t-1)n_{\text{g}}+i}\right) \tag{1}$$

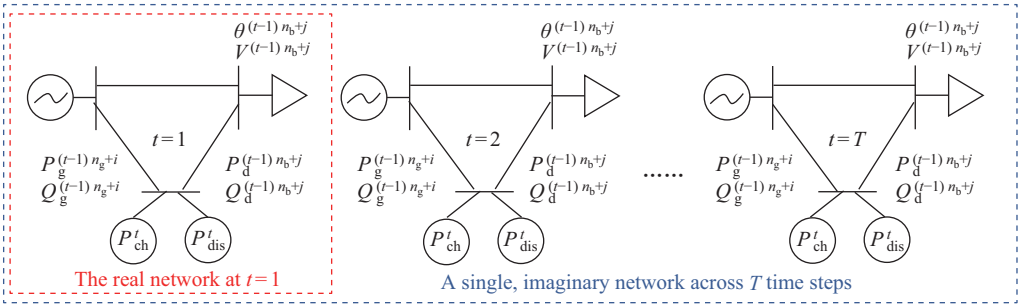

Fig. 1. Integration of the simplified networks across T time steps into a single imaginary network for the DOPF implementation.

Subject to:

$$g_{\mathrm{P}}(\theta^{*t}, V^{*t}, P_{\mathrm{d}}^{*t}, P_{\mathrm{g}}^{(t-1)\cdot n_{\mathrm{g}}+i}, P_{\mathrm{ch}}^{t}, P_{\mathrm{dis}}^{t}) = 0 \ \forall t \quad (2)$$

$$g_{\mathrm{Q}}(\theta^{*t}, V^{*t}, Q_{\mathrm{d}}^{*t}, Q_{\mathrm{g}}^{(t-1)\cdot n_{\mathrm{g}}+i}) = 0 \ \forall t \quad (3)$$

$$|S_{\mathrm{fr}}(\theta^{*t}, V^{*t})| - \overline{S} \leq 0 \ \forall t \quad (4)$$

$$|S_{\mathrm{to}}(\theta^{*t}, V^{*t})| - \overline{S} \leq 0 \ \forall t \quad (5)$$

$$\underline{X} \leq X \leq \overline{X} \quad (6)$$

$$h_{\mathrm{G}}\left(P_{\mathrm{g}}^{(t-1)\cdot n_{\mathrm{g}}+i}\right) \leq 0 \ \forall t \quad (7)$$

$$h_{\mathrm{B}}\left(P_{\mathrm{ch}}^{t}, P_{\mathrm{dis}}^{t}\right) \leq 0 \ \forall t \quad (8)$$

where superscript $(*t)$ represents $(j + (t-1)n_{\mathrm{b}})$; $g_{\mathrm{P}}(\cdot)$ and $g_{\mathrm{Q}}(\cdot)$ denote active and reactive power balance equations for each bus, respectively; $S_{\mathrm{fr}}(\cdot)$ and $S_{\mathrm{to}}(\cdot)$ calculate apparent powers at the "from" and "to" ends of each branch, respectively, which must not exceed the branch flow limit $\overline{S}$ in magnitude; $\underline{X}$ and $\overline{X}$ signify the minimum and maximum limits on X, respectively; and (7) and (8) reflect the additional operational constraints specified for the generators and BESS, which are explained in Sections II.B and II.C, respectively. Noticeably, the virtual generators modeling imports/exports of the BESS are treated as zero-cost generators. Although they are excluded from the objective function (1), the cost of cycling the BESS is reflected by the energy losses, which in turn are measured by the round-trip efficiency of the BESS.

To accomplish the objective of reducing the predicted power curtailment of RGs, here, the $f_{\mathrm{g}}^{i}(\cdot)$ of RGs is defined by zero, which stimulates power injections from the zero-cost RGs, and promotes the absorption of forecast curtailment by BESS, subsequently putting it onto the network at peak times. For the BESS with a round-trip efficiency η_{B}, the outputs of conventional generators (CGs) are shifted when the CG cost of charging the BESS by, for instance, 1 MWh is smaller than the savings in the CG cost by the BESS exporting $1 \times \eta_{\mathrm{B}}$ MWh, which would otherwise be supplied by the CGs. When $f_{\mathrm{g}}^{i}(\cdot)$ of a CG is defined as the x^{th} power of the real power, its incremental cost of producing an additional unit of electricity is the derivative of $f_{\mathrm{g}}^{i}(\cdot)$ with respect to the real power, i.e., the $(x-1)^{\mathrm{th}}$ power of the real power. Hence, the BESS is expected to shift the conventional generation given the ratio between high and low export of a CG exceeds at least by $\sqrt[(x-1)]{1/\eta_{\mathrm{B}}}$. Here, since the BESS with η_{B} of 75% is designed to shift the CG export when the ratio between high and low CG export is greater than 1.1, $f_{\mathrm{g}}^{i}(\cdot)$ of CGs are set as the 4^{th} power of real power (i.e., $x = 4$ leading to $\sqrt[3]{1/75\%} \approx 1.1$). The CG outputs can be smoothed out further by defining $f_{\mathrm{g}}^{i}(\cdot)$ with a higher-order power of its real power.

The generation cost functions defined here for RGs, CGs, and the BESS-related virtual generators allow the DOPF to concentrate heavily on mitigating the RG curtailment, followed by smoothing the CG export, given a particular degree of the export variation. A BESS cycle is implemented only if the zero-cost RG is to be curtailed and/or the CG export variation exceeds the target degree, i.e., the cost of charging the BESS is found to be lower than the cost of the CG displaced by the BESS export over a plan time horizon. Although the modeling of the investment cost or the lifetime loss (or degradation) of a BESS is essential to invest in a BESS project and/or evade an excessive utilization of battery causing a costlier loss in lifetime [26], they are not considered for this paper. The reason being that this paper develops the DOPF to deal with the day-ahead schedule or operational issues of a BESS and aims to fully exploit the available energy capacity of the BESS over each cycle given the warranty covering the maintenance within a specific number of cycles. If the capacity fade of a BESS is available to the operators through a BESS management system [27], the remaining energy capacity of the BESS could be updated in the DOPF at the onset of the day-ahead scheduling.

B. Operational Constraints on 33 kV Network

The 33 kV network analyzed in this paper is supplied by two conventional generators, CG_1 and CG_2, which provide the base load and the spinning reserve, respectively. Four wind farms are located across the network: a 3.7 MW wind farm (WF_1) with a firm or must-take network connection and three non-firm wind farms (denoted by WF_2, WF_3, and WF_4, respectively), which bear a total capacity of 8 MW and are connected under flexible contracts to the network. A 1 MW grid-scale BESS is placed on the network to execute the time shift of non-firm wind and conventional generation.

Two specific operational constraints are introduced here to ensure that CG_1 contributes at least 40% of the total generation and that the spinning reserve provided by CG_2 is sufficient to compensate for the loss of all wind generation at each instant. These are formulated by (9) and (10), where, $P_{\mathrm{g}}^{\mathrm{CG}_1}$, $P_{\mathrm{g}}^{\mathrm{CG}_2}$, and $P_{\mathrm{g}}^{\mathrm{WF}_w}$ denote the real powers of CG_1, CG_2, and WF_w $(w = 1, \cdots, 4)$, respectively, and $\overline{P}_{\mathrm{g}}^{\mathrm{CG}_2}$ represents the maximum limit on $P_{\mathrm{g}}^{\mathrm{CG}_2}$, i.e., 20 MW. In times of low system demand coinciding with high wind periods, the non-firm wind generation is likely to be curtailed, to evade breaching the two operational constraints.

$$0.4P_{\mathrm{g}}^{\mathrm{CG}_2} + 0.4\sum_{w=1}^{4} P_{\mathrm{g}}^{\mathrm{WF}_w} - 0.6P_{\mathrm{g}}^{\mathrm{CG}_1} \leq 0 \quad (9)$$

$$P_{\mathrm{g}}^{\mathrm{CG}_2} + \sum_{w=1}^{4} P_{\mathrm{g}}^{\mathrm{WF}_w} \leq \overline{P}_{\mathrm{g}}^{\mathrm{CG}_2} \quad (10)$$

The operational constraints formulated in (9) and (10) are incorporated into DOPF as inequality constraints related to (7). The export limits of CG_1 and CG_2 together with available power forecasts of non-firm wind farms across T time steps are taken into account in (6). For the firm WF_1, the maximum and minimum limits on the export are both equal to the predicted available power, such that all its power is injected into the network. Here, the time-varying load at each bus is approximated as a product of the load capacity at that particular bus and the normalized data, which is extracted from the time series of the total system demand on the network.

C. Operational Constraints on BESS

As noted in Section II.A, the state of charge (SOC) of a BESS remains an inter-temporal variable that connects the networks across T time steps over a plan time horizon. The

SOC at the end of a particular time step t, denoted by SOC_{t}, is calculated by:

$$SOC_{\mathrm{t}} = SOC_0 - \frac{\Delta t}{C_{\mathrm{B}}^{\mathrm{r}}} \sum_{\tau=1}^{t} \left(\eta_{\mathrm{ch}} P_{\mathrm{ch}}^{\tau} + \frac{P_{\mathrm{dis}}^{\tau}}{\eta_{\mathrm{dis}}} \right) \tag{11}$$

where SOC_0 is the initial SOC at the start of the plan time horizon; $C_{\mathrm{B}}^{\mathrm{r}}$ represents the rated energy capacity of the BESS; Δt denotes the time step length (i.e., 15 minutes here); and η_{dis} and η_{ch} are the discharge and charge efficiencies, respectively. Further, SOC_{t} is constrained by the minimum and maximum SOC levels (i.e., $\underline{SOC}$ and $\overline{SOC}$), leading to:

$$\frac{t}{C_{\mathrm{B}}^{\mathrm{r}}} \sum_{\tau=1}^{t} \left(\eta_{\mathrm{ch}} P_{\mathrm{ch}}^{\tau} + \frac{P_{\mathrm{dis}}^{\tau}}{\eta_{\mathrm{dis}}} \right) \leq (SOC_0 - \underline{SOC}) \ \forall t \tag{12}$$

$$-\frac{t}{C_{\mathrm{B}}^{\mathrm{r}}} \sum_{\tau=1}^{t} \left(\eta_{\mathrm{ch}} P_{\mathrm{ch}}^{\tau} + \frac{P_{\mathrm{dis}}^{\tau}}{\eta_{\mathrm{dis}}} \right) \leq (\overline{SOC} - SOC_0) \ \forall t \tag{13}$$

Unlike a discharging phase where P_{dis}^{t} is constantly limited by the rated power $P_{\mathrm{B}}^{\mathrm{r}}$ (i.e., $0 \leq P_{\mathrm{dis}}^{t} \leq P_{\mathrm{B}}^{\mathrm{r}}$), the charging phase is usually regulated based on a specific charging method [22]. One of the most prevalent methods is a CC-CV profile (see Fig. 2(a)), where a BESS can constantly import at $P_{\mathrm{B}}^{\mathrm{r}}$ until its SOC increases to a particular level— SOC_{C}, which results in the battery voltage reaching its maximum allowable level at time t_{C}; then, the import rate exponentially declines with time to a predefined cut-off rate $P_{\mathrm{B}}^{\mathrm{co}}$, until the BESS realizes its full charge at time t_{E} to maintain a constant voltage at the maximum allowable level [22], [28]. The open circuit voltage of the battery varying with its SOC [29] may not ensure a strictly constant limit on the import rate at the CC stage. Enabling the formulation of CC-CV profile in the DOPF, a constant $P_{\mathrm{B}}^{\mathrm{r}}$ is introduced here over the CC stage, as shown in Fig. 2.

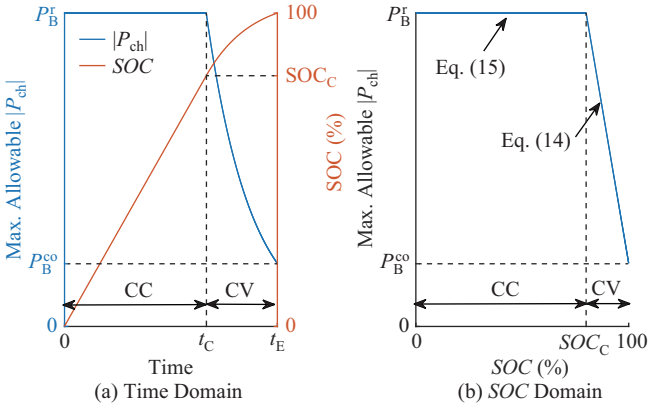

Fig. 2. CC-CV charging profiles in (a) time and (b) SOC domains.

In general, the CC-CV method presumes that a BESS constantly follows the charging profile in time, which is impractical in terms of the scheduling problem for the work conducted in this paper. To facilitate functional relevance of the CC-CV method, we convert the charging profile from the time domain to the SOC domain (see Fig. 2(b)) by proving that, in the CV stage, the exponential decline of the maximum allowable charge rate with time is equivalent to a linear decrease with the SOC at a rate of $\alpha = (P_{\mathrm{B}}^{\mathrm{co}} - P_{\mathrm{B}}^{\mathrm{r}})/(1 - SOC_{\mathrm{C}})$. Given SOC_{t-1} at the end of the time step $(t-1)$ modeled by (11), the CC-CV-related limits on P_{ch}^{t} in the following time step t can be formulated in (14) and (15), which illustrate the boundaries defined by two straight lines in Fig. 2(b), respectively.

$$-P_{\mathrm{ch}}^{t} + \frac{\alpha t}{C_{\mathrm{B}}^{\mathrm{r}}} \sum_{\tau=1}^{t-1} \left(\eta_{\mathrm{ch}} P_{\mathrm{ch}}^{\tau} + \frac{P_{\mathrm{dis}}^{\tau}}{\eta_{\mathrm{dis}}} \right) \leq P_{\mathrm{B}}^{\mathrm{r}} + \alpha(SOC_0 - SOC_{\mathrm{C}}) \ \forall t \tag{14}$$

$$-P_{\mathrm{B}}^{\mathrm{r}} \leq P_{\mathrm{ch}}^{t} \leq 0 \ \forall t \tag{15}$$

The operational limits on BESS formulated in (12)–(14) and (15) are taken into account for the DOPF as inequality constraints, related to (8) and (6), respectively. The BESS parameters required for the modeling are as listed in Table I.

TABLE I
PARAMETERS OF THE BESS FOR THE MODELING

Parameter	Value	Parameter	Value
$P_{\mathrm{B}}^{\mathrm{r}}$	1 MW	$C_{\mathrm{B}}^{\mathrm{r}}$	6.34 MWh
$\underline{SOC}$	45%	$\overline{SOC}$	100%
η_{dis}	86.1%	η_{ch}	87.1%
$P_{\mathrm{B}}^{\mathrm{co}}$	0.33 MW	SOC_{C}	80%

III. Scheduling Framework with Wind Input Modeling

A. DOPF-based Scheduling Framework

Although the generation can be more cost-effective if multiple small cycles are implemented over a plan time horizon, this could result in the escalated degradation of a battery's lifetime [30]. In addition, the minimum SOC level $\underline{SOC}$ of the BESS is set to 45% (see Table I), to reduce the battery degradation caused by large SOC variations [31]. The BESS generally has a warranty that covers the maintenance until reaching a specified number of cycles. Therefore, optimum utilization of the available energy capacity (i.e., 45% SOC–100% SOC) of the BESS over each cycle is preferred for the work conducted in this paper. Due to the timing of peak demand on the network (i.e., two peak periods over 5:00–9:00 and 13:00–18:00 on an average, which are separated by around 4 hours) and the durations that were required for discharging and charging phases (i.e., at least 3 hours and 5 hours under a CC-CV curve, respectively), the BESS could rationally only perform a complete cycle per day. Taking into account these realistic requirements, a scheduling framework is developed based on DOPF to optimize a full battery cycle in a day(s)-ahead schedule.

In this framework, a plan time horizon is defined as the time period from the time step $(t = 1)$ following the previous full cycle (i.e., the time step before which the BESS is just discharged to $\underline{SOC}$ in the previous plan time horizon) to the final time step $(t = T)$ in the subsequent day(s). Subsequently, the plan time horizon is split by a particular time point into charging and discharging periods, within which export rates and import rates are forced to zero, respectively, to fulfil the single-cycle requirement per day. The morning peaks on the network usually occurred at around 5:00–9:00, where

the discharging period would start. Nonetheless, since wind generation would influence the peak demands to be met by CGs, in this study, each time point in the first 12 hours of the final day is adopted as a potential split time point with an index k ($k = 1, \cdots, 49$), which defines that the discharging period starts at the time step $t_{\text{dis}} = (T - 96 + k)$. Fig. 3 demonstrates an example of splitting a 27-hour time horizon (i.e., $T = 108$) at 5:00 (i.e., $k = 21$ with $t_{\text{dis}} = 33$). Then, P^t_{dis} in the charging period and P^t_{ch} in the discharging period are all limited to zero, to constraint the BESS to carry out a single cycle in the plan time horizon. This is achieved by employing (16) and (17), which are expressed in the DOPF as inequality constraints related to (8).

$$\sum_{\tau=1}^{t_{\text{dis}}-1} (P^{\tau}_{\text{dis}}) \leq 0 \tag{16}$$

$$-\sum_{\tau=t_{\text{dis}}}^{T} (P^{\tau}_{\text{ch}}) \leq 0 \tag{17}$$

Based on available wind power and system demand across T time steps, the optimal schedules of all the network components are calculated by DOPF for each potential split point. If the BESS was not fully charged before the discharging period in any schedule (i.e., $SOC_{t_{\text{dis}}-1} < 1 \ \forall k$), the horizon would be extended to include the next 24 hours, totally comprising $(T + 96)$ time steps; then, DOPF is applied to the new horizon. The schedule resulting in a 100% $SOC_{t_{\text{dis}}-1}$ and the smallest overall generation cost is finally selected. A flow chart illustrating the DOPF-based scheduling framework is shown in Fig. 4.

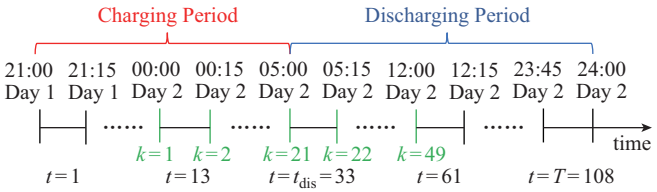

Fig. 3. A 27-hour plan time horizon (i.e., $T = 108$) from 21:00 on day 1 to 24:00 on day 2 being split at 05:00 on day 2 ($k = 21$).

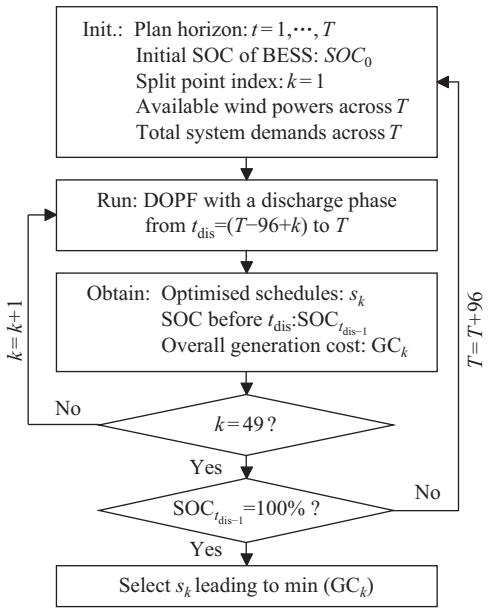

Fig. 4. A flow chart showing the DOPF-based scheduling framework.

B. Modeling of Available Wind Generation

The available powers $\overline{P}_{\text{W}}$ of wind farms on the network, i.e., an input of DOPF, are estimated based on wind speeds v_{h} at hub heights combined with a generic power curve model [32], which is employed here to deduce the power curves from the available technical parameters for wind turbines at WF_1 [33], [34], WF_2 [35], WF_3 [36], and WF_4 [35], respectively:

$$\overline{P}_{\text{W}} = \begin{cases} 0 & \text{for} \quad v_{\text{h}} \leq v_i \\ P^{\text{r}}_{\text{W}}(a + bv_{\text{h}} + cv^2_{\text{h}}) & \text{for} \quad v_i < v_{\text{h}} \leq v_{\text{r}} \\ P^{\text{r}}_{\text{W}} & \text{for} \quad v_{\text{r}} < v_{\text{h}} \leq v_{\text{o}} \\ 0 & \text{for} \quad v_{\text{h}} > v_{\text{o}} \end{cases} \tag{18}$$

where P^{r}_{W} is the rated power of the wind turbine. v_i, v_{r}, and v_{o} represent the cut-in, rated, and cut-out wind speeds for a wind turbine, respectively, and constants a, b, and c are only subject to v_i and v_{r} [32]:

$$a = -\frac{v_i(v_i + v_{\text{r}})(v_i^2 + 2v_iv_{\text{r}} - v_{\text{r}}^2)}{2(v_i - v_{\text{r}})^2 v_{\text{r}}^2} \tag{19}$$

$$b = \frac{v_i^4 + 4v_i^3v_{\text{r}} + 6v_i^2v_{\text{r}}^2 - 2v_iv_{\text{r}}^3 - v_{\text{r}}^4}{2(v_i - v_{\text{r}})^2 v_{\text{r}}^3} \tag{20}$$

$$c = -\frac{v_i^3 + 3v_i^2v_{\text{r}} + 3v_iv_{\text{r}}^2 - 3v_{\text{r}}^3}{2(v_i - v_{\text{r}})^2 v_{\text{r}}^3} \tag{21}$$

The v_{h} at the hub height of each wind farm is estimated from hourly wind speeds measured at the surrounding five MIDAS (Met Office Integrated Data Archive System) stations [23] by employing an inverse distance weighting (IDW) interpolation method and modeling the influence of the ground roughness on the wind speed [37], [38]:

$$v_{\text{h}} = \frac{\ln(z_{\text{h}}/r_{\text{h}})}{\ln(z^{\text{h}}_{\text{r}}/r_{\text{h}})} \sum_{l=1}^{5} \left(v^{\text{l}}_{\text{m}} \frac{\ln(z^{\text{l}}_{\text{r}}/r^{\text{l}}_{\text{m}})}{\ln(z^{\text{l}}_{\text{m}}/r^{\text{l}}_{\text{m}})} \frac{1/{d^{\text{l}}_{\text{m}}}^2}{\sum_{l=1}^{5}\left(1/{d^{\text{l}}_{\text{m}}}^2\right)} \right) \tag{22}$$

where d^{l}_{m} is the horizontal distance from a particular wind farm to the l^{th} ($l = 1, \cdots, 5$) MIDAS station. r_{h} and r^{l}_{m} denote ground roughness lengths at the wind farm and the l^{th} MIDAS station, respectively, based on which the wind speed measurements v^{l}_{m} at the anemometer heights z^{l}_{m} above ground level (AGL) are first converted to a selected reference level z^{l}_{r} AGL by adopting a log-law wind profile [37]. Subsequently, the IDW is applied to estimate the interpolation result for the wind farm at the reference level z^{h}_{r} AGL, which is converted to the hub height z_{h} AGL to get v_{h}. Several available reference levels, e.g., $\geq$ 200 m AGL or above sea level (ASL), have been tested through a cross-validation procedure [38], [39], where each MIDAS station is deemed as the target location. Based on the average interpolation performance in terms of root mean square error, a reference level of 200 m ASL is adopted here, such that z^{h}_{r} and z^{l}_{r} are the deviations of the altitudes of the wind farm and MIDAS stations from 200 m

ASL.

Based on the modeled $\overline{P}_{\mathrm{W}}$, WF_1 sharing a firm connection with the network is estimated to bear a capacity factor of around 56%. This is slightly higher than the recorded capacity factor of 52%, partly due to the fact that the modeling approach devised in this study does not consider wind turbine outages. The similar capacity factors indicate that the modeled $\overline{P}_{\mathrm{W}}$ can be employed here as a reasonable approximation for testing the scheduling framework. The hourly $\overline{P}_{\mathrm{W}}$ are then converted to 15-minute intervals in line with Δt in DOPF.

IV. Results and Model Validation

All the mathematical calculations incorporated in this paper are undertaken using MATLAB [40]. The DOPF-based scheduling framework is implemented in conjunction with MATPOWER [41] based on the available modeled wind powers and the time-varying load at each bus across a plan time horizon. The optimized real powers of the two virtual generators that model the imports and exports of the BESS are merged together to acquire the BESS schedule. The optimized schedules are analyzed under the context of the incorporation of CC-CV profile, the mitigation of wind curtailment, the smoothing of conventional generation, and the optimum utilization of the available energy capacity of the BESS in each cycle. Considering that the primary focus of this paper is the effectiveness of the developed scheduling framework, the scheduling process is applied to historical data of system demand and available wind power estimates instead of their forecasts in this study.

A. Assessment on Time-shift of Non-firm Wind Generation

The non-firm wind farms (NFWFs) on the 33 kV network are highly likely to diminish their power outputs over high wind periods that coincide with low system demand, to maintain the network stability under the operational constraints, as described in Section II.B. To quantify the non-firm wind generation to be curtailed without the BESS cycling, power outputs of all generating units are dispatched for each time step by adopting the DOPF, where the virtual generators modeling the BESS and the operational constraints on the BESS are removed. Fig. 5 illustrates the first 8 hours of a particular 24-hour time horizon from 19:00 on Day 4 to 19:00 on Day 5 during which the total available power outputs $\sum \overline{P}_{\mathrm{NF}}$ of NFWFs exceeded the constraints determined by (9) and (10) for most of that time period. Driven by the minimization of the overall generation cost, the BESS is scheduled by DOPF to import at times of the anticipated curtailment, to alleviate the limit on $\sum \overline{P}_{\mathrm{NF}}$ (see Fig. 5), and then export at peak times, as shown in Fig. 6.

The day-ahead schedule in Fig. 6 demonstrates that the BESS completes a full cycle as required in this study, with import rates being maintained within the range of CC-CV-related constraints that are calculated from the CC-CV charging profile represented in the SOC domain (see Fig. 2(b)). The import rates of the BESS and the reduced wind curtailment are compared in Fig. 7, where only around 60% of the energy absorbed by the BESS is obtained from the otherwise curtailed

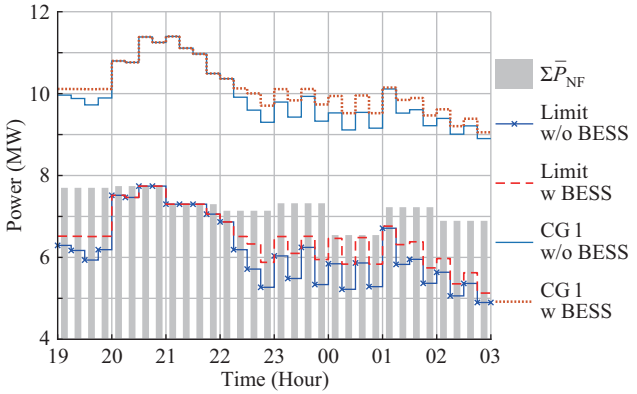

Fig. 5. The aggregated available non-firm wind generation $\sum \overline{P}_{\mathrm{NF}}$ and the limits determined by (9) and (10) along with power outputs of CG_1 from 19:00 on Day 4 to 03:00 on Day 5.

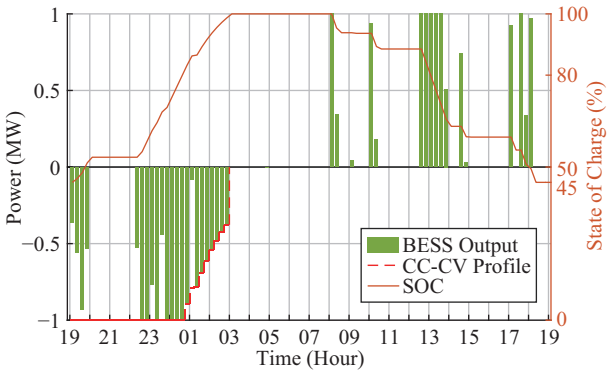

Fig. 6. The schedule of the BESS and the SOC-dependent limits on import rates related to the CC-CV profile from 19:00 on Day 4 to 19:00 on Day 5.

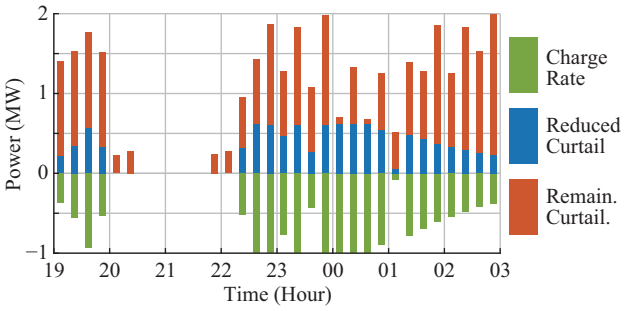

Fig. 7. Import rates of BESS and otherwise curtailed wind generation absorbed by the BESS from 19:00 on Day 4 to 03:00 on Day 5.

wind generation. This is because the constraints on $\sum \overline{P}_{\mathrm{NF}}$ over this period are found to be consistently dominated by (9), which requires CG_1 to contribute at least 40% of the total system generation. Therefore, in this case, the import of the BESS also boosts the power output of CG_1, as shown in Fig. 5. Since CG_1 generating at a lower level has a smaller incremental cost per MWh, the BESS generally imports at a higher rate when the wind curtailment coincides with a lower export of CG_1. For example, although the wind curtailment would exceed 0.6 MW in both 19:00–20:00 and 23:45–00:45, the BESS is charged at 1 MW for the latter 1-hour period only (see Fig. 7), where the CG_1 export is observed to be much lower (see Fig. 5). Furthermore, it is found that the electricity

used to charge the BESS is smaller than the increase of total system generation due to transmission losses.

B. Assessment on Time-shift of Conventional Generation

In the plan time horizons where NFWFs are to be slightly or not curtailed, the schedules of the BESS are determined by the differences occurring in incremental generation costs of CGs among T time steps. The BESS having a round-trip efficiency η_{B} of 75% in this study is cycled if the incremental generation costs of CGs at high export levels are greater than $1/75\% \approx 1.33$ times as much as those at low export levels, without considering the power losses on the transmission cables. As noted in Section II.A, the incremental costs of CGs are dependent on the cube of their active power outputs in the DOPF developed in this study. Therefore, the export of CG_1 and CG_2 is shifted by the BESS given that the ratio between high and low active power outputs exceeds $\sqrt[3]{1.33} \approx 1.1$. Noticeably, this ratio increases when transmission losses are included.

Figure 8 compares the aggregated export of CGs dispatched by using the DOPF without the BESS operation against those that are smoothed by the DOPF-based BESS cycle over a particular 24-hour time horizon from 19:00 on Day 1 to 19:00 on Day 2, where NFWFs are not curtailed. The significant differences in aggregated MW outputs of CGs, e.g., between 22:45–03:00 and 06:00–08:30, are observed to be minimized by the BESS cycle. Additionally, BESS is designed to import (or export) at a higher rate subject to the maximum allowable limit associated with the CC-CV curve (or the rated power $P_{\mathrm{B}}^{\mathrm{r}}$) at times of CGs exporting at a lower (or higher) level, e.g., during 01:45–03:00 (or 07:30–08:30). In this manner, the system demand to be supplied by CGs can be smoothed to a great extent, minimizing the overall generation cost across the plan time horizon.

C. Assessment on Utilization of Available Energy Capacity of BESS

As described in Section III.A, the scheduling framework implements the DOPF for each potential split time point, which divides a plan time horizon into charging and discharging periods, to meet the pragmatic requirement of completing one cycle per day in the plan time horizon. If there are available schedules where the BESS is completely charged up to the split point, the schedule leading to the least overall generation cost is selected to operate the BESS; otherwise, the plan time horizon is extended to include the following 96 quarter-hour time steps until the available energy capacity of BESS is fully utilized in the schedule. Fig. 9 demonstrates the outputs of the BESS and CGs scheduled by DOPF over a plan time horizon from 22:30 on Day 48 to 24:00 on Day 49 during which NFWFs exporting at low levels are not curtailed. Although the use of a split point at 12:00 provides the longest charging period of 13.5 hours in this case, the BESS performs an incomplete cycle, with the SOC reaching 71.3% only at the split point due to the relatively small variation in conventional generation. It is found that the maximum/minimum of CG_1 and CG_2 outputs at times of the BESS discharging/charging at less than 1 MW is

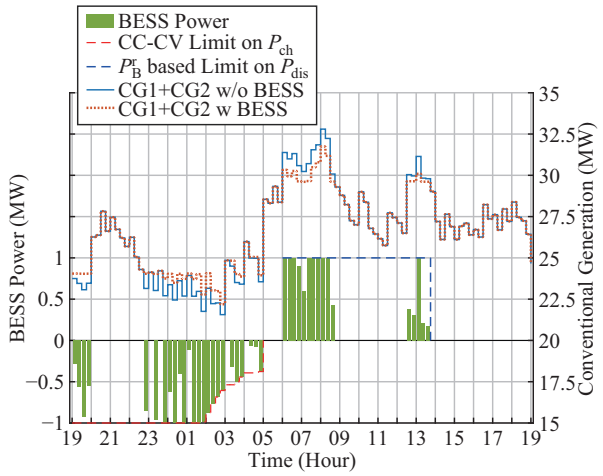

Fig. 8. Aggregated power outputs (MW) of CGs dispatched with or without a complete battery cycle during a 24-hour time horizon from 19:00 on Day 1 to 19:00 on Day 2.

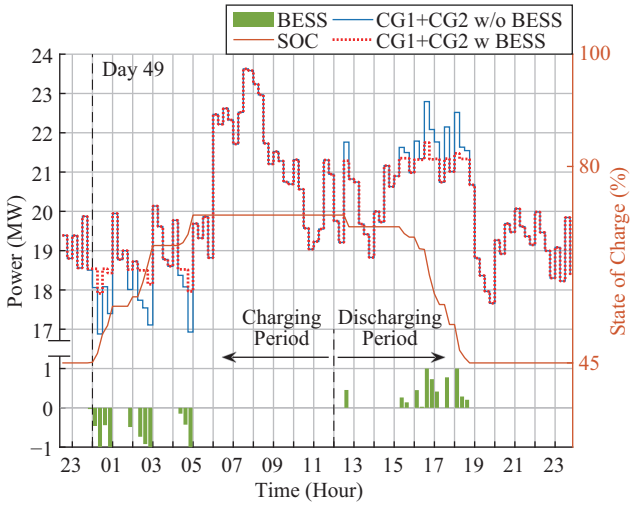

Fig. 9. Aggregated power outputs (MW) of CGs dispatched with or without an incomplete battery cycle over a plan horizon form 22:30 on Day 48 to 24:00 on Day 49.

10.28 MW/8.91 MW and 11.05 MW/9.59 MW, respectively, with both having a ratio of around 1.15. This is slightly higher than the ratio of $\sqrt[3]{1.33} \approx 1.1$, beyond which the BESS with η_{B} of 75% is expected to shift the conventional generation due to transmission losses, as noted in Section IV.B. It appears that the schedule of an incomplete battery cycle is likely to occur when the NFWFs export at low levels and CGs have flat power outputs in the plan time horizon.

Since no schedule over the plan horizon, as depicted in Fig. 9, can offer a full BESS cycle execution, the BESS operation is re-scheduled in an extended horizon, which terminates at 24:00 on Day 50. The new horizon offers a longer period for the BESS charging and increases the likelihood of maximizing the utilization of available energy capacity of the BESS. The 2-day-ahead schedules of the BESS and conventional generation in the new plan time horizon are plotted in Fig. 10 (the time period with a complete battery cycle from 22:30 on Day 48 to 19:00 on Day 50 is shown). The BESS is scheduled to import during demand troughs of the two days and reach the full

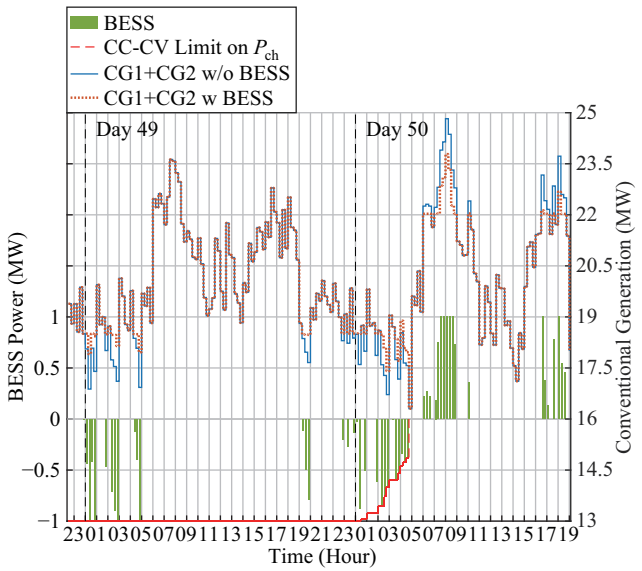

Fig. 10. Aggregated power outputs (MW) of CGs dispatched with or without a full battery cycle over an extended plan horizon from 22:30 on Day 48 to 24:00 on Day 50.

100% SOC before the morning peak on Day 50, thereby fulfilling the pragmatic requirement of completely utilizing the available energy capacity of BESS. The scheduling framework has been examined based on the data for a span of two-years, realizing that the BESS is designed to perform a complete cycle in each plan time horizon.

V. Conclusions and Future Work

Grid-scale battery energy storage systems (BESS) are conducive to achieving flexible and low carbon operation of modern electrical networks. Unlike the BESS designed to respond to the deviation of a specific system variable (e.g., frequency) from an expected level in real-time, the BESS applied to the shifting of renewable and conventional generation typically requires forecasting an optimal schedule that determines the best time periods and volumes for charging and discharging in advance. To meet this increasing demand, in this paper we developed a dynamic Optimal Power Flow (DOPF)-based scheduling framework to optimize the day(s)-ahead operation of a 1 MW BESS, to mitigate the predicted curtailment of non-firm wind generation and smooth out the system demand supplied by the conventional generating units on a particular 33 kV network. In addition to the traditionally formulated inter-temporal constraints that maintain the state of charge (SOC) of the BESS within the maximum and minimum levels, a constant current-constant voltage (CC-CV) charging profile converted from the time domain to the SOC domain has been incorporated into the DOPF to limit the import rate of the BESS in this study.

To fulfil the practical requirements of optimally utilizing the available energy capacity of the BESS and completing a full cycle up to once per day, the scheduling framework developed here splits a plan time horizon into charging and discharging periods at each potential instant, and then selects the schedule that results in a 100% SOC at the split time point with the least overall generation cost, or extends the plan time horizon if the BESS is not fully charged at the split time point in any schedule optimized by the DOPF. The effectiveness of the scheduling framework has been discussed based on the day(s)-ahead schedules over three particular plan time horizons, i.e., a high wind period and two low wind periods, in concurrence with relatively significant and small diurnal changes of conventional generation, respectively. By defining the incremental costs of wind and conventional generation as zero and a cube of active power, respectively, the schedules have alleviated the forecast limits on the non-firm wind generation, and shifted the conventional generation, given that the ratio between high and low active power outputs exceeds the cube root of the reciprocal of the round-trip efficiency of BESS. Furthermore, the scheduling framework has effectively exhibited its capability of maximizing the utilization of available energy capacity of the BESS in each cycle as required.

In light of the existing work, predictions of available wind power outputs and system demand for day(s)-ahead should be estimated by using the numerical weather prediction and statistical models, and taken into the scheduling framework to investigate the impacts of forecast errors on the performance of day(s)-ahead schedules in terms of the alleviated wind curtailment and the shifted conventional generation. The CC-CV profile in the SOC domain also requires further enhancement to reflect the influence of the SOC-dependent open circuit voltage of the battery. In addition, the scheduling framework could be developed further to deal with the forecast uncertainties and incorporate other inter-temporal technologies, such as demand side management and different energy storage systems. Furthermore, capital and operating cost (and the degradation mechanisms, if applicable) of these technologies should be modeled as well to estimate their optimal sizes (MW, MWh) that lead to significant factors, such as the maximum amount of the reduced wind curtailment per unit cost during their lifetime. This will enable the determination of the most appropriate technology or combination of technologies, facilitating efficient project planning and investment.

Acknowledgment

The authors gratefully acknowledge the supply of weather data from British Atmospheric Data Centre.

References

[1] White Paper Electricity Energy Storage, "International electrotechnical commission," Geneva, Switzerland, Tech. Rep., 2013.

[2] J. H. Li, Y. N. Fu, C. P. Li, J. Li, Z. T. Xing, and T. Ma, "Improving wind power integration by regenerative electric boiler and battery energy storage device," *International Journal of Electrical Power & Energy Systems*, vol. 131, pp. 107039, Oct. 2021.

[3] A. Barzkar and S. M. H. Hosseini, "A novel peak load shaving algorithm via real-time battery scheduling for residential distributed energy storage systems," *International Journal of Energy Research*, vol. 42, no. 7, pp. 2400–2416, Jun. 2018.

[4] F. L. Fan, G. Zorzi, D. Campos-Gaona, G. Burt, O. Anaya-Lara, J. Nwobu, and A. Madariaga, "Sizing and coordination strategies of battery energy storage system Co-located with wind farm: the UK perspective," *Energies*, vol. 14, no. 5, pp. 1439, Mar. 2021.

[5] C. P. Li, H. Y. Zhou, J. H. Li, and Z. M. Dong, "Economic dispatching strategy of distributed energy storage for deferring substation expansion in the distribution network with distributed generation and electric vehicle," *Journal of Cleaner Production*, vol. 253, pp. 119862, Apr. 2020.

[6] A. D. Del Rosso and S. W. Eckroad, "Energy storage for relief of transmission congestion," *IEEE Transactions on Smart Grid*, vol. 5, no. 2, pp. 1138–1146, Mar. 2014.

[7] J. L. Li, Z. J. Du, R. E. Ruther, S. J. An, L. A. David, K. Hays, M. Wood, N. D. Phillip, Y. P. Sheng, C. Y. Mao, S. Kalnaus, C. Daniel, and D. L. Wood III, "Toward low-cost, high-energy density, and high-power density lithium-ion batteries," *JOM*, vol. 69, no. 9, pp. 1484–1496, Jun. 2017.

[8] X. J. Li and S. X. Wang, "Energy management and operational control methods for grid battery energy storage systems," *CSEE Journal of Power and Energy Systems*, vol. 7, no. 5, pp. 1026–1040, Sep. 2021.

[9] "A good practice guide on electricity energy storage," EA Technology, Chester, UK, Tech. Rep., 2014.

[10] X. J. Li, D. Hui, and X. K. Lai, "Battery energy storage station (BESS)-based smoothing control of photovoltaic (PV) and wind power generation fluctuations," *IEEE Transactions on Sustainable Energy*, vol. 4, no. 2, pp. 464–473, Apr. 2013.

[11] A. Sattar, A. Al Durra, C. Caruana, S. M. Muyeen, and J. Tamura, "Real-time implementation of BESS to smooth the output power fluctuation of variable speed wind turbine generator," *IEEJ Journal of Industry Applications*, vol. 3, no. 3, pp. 198–205, May 2014.

[12] F. J. Lin, H. C. Chiang, J. K. Chang, and Y. R. Chang, "Intelligent wind power smoothing control with BESS," *IET Renewable Power Generation*, vol. 11, no. 2, pp. 398–407, Feb. 2017.

[13] C. Q. Ju and P. Wang, "Dynamic optimal power flow including energy storage with adaptive operation costs," in *Proceedings of the 41st Annual Conference of the IEEE Industrial Electronics Society*, Yokohama, Japan, 2015, pp. 1561–1566.

[14] S. Chakraborty, T. Senjyu, H. Toyama, A. Y. Saber, and T. Funabashi, "Determination methodology for optimising the energy storage size for power system," *IET Generation, Transmission & Distribution*, vol. 3, no. 11, pp. 987–999, Nov. 2009.

[15] I. Lampropoulos, P. Garoufalis, P. P. J. van den Bosch, R. J. W. de Groot, and W. L. Kling, "Day-ahead economic scheduling of energy storage," in *Proceedings of 2014 Power Systems Computation Conference*, 2014, pp. 1–7.

[16] N. Li, C. Uçkun, E. M. Constantinescu, J. R. Birge, K. W. Hedman, and A. Botterud, "Flexible operation of batteries in power system scheduling with renewable energy," *IEEE Transactions on Sustainable Energy*, vol. 7, no. 2, pp. 685–696, Apr. 2016.

[17] S. Gill, I. Kockar, and G. W. Ault, "Dynamic optimal power flow for active distribution networks," *IEEE Transactions on Power Systems*, vol. 29, no. 1, pp. 121–131, Jan. 2014.

[18] Z. Cai, C. Bussar, P. Stöcker, L. Jr. Moraes, D. Magnor, and D. U. Sauer, "Optimal dispatch scheduling of a wind-battery-system in German power market," *Energy Procedia*, vol. 99, pp. 137–146, Nov. 2016.

[19] H. W. Dommel and W. F. Tinney, "Optimal power flow solutions," *IEEE Transactions on Power Apparatus and Systems*, vol. PAS-87, no. 10, pp. 1866–1876, Oct. 1968.

[20] P. W. Chen, X. N. Xiao, and X. H. Wang, "Dynamic optimal power flow model incorporating interval uncertainty applied to distribution network," *IET Generation, Transmission & Distribution*, vol. 12, no. 12, pp. 2926–2936, Jul. 2018.

[21] W. L. Bai, D. Lee, and K. Y. Lee, "Stochastic dynamic AC optimal power flow based on a multivariate short-term wind power scenario forecasting model," *Energies*, vol. 10, no. 12, pp. 2138, Dec. 2017.

[22] I. H. Cho, P. Y. Lee, and J. H. Kim, "Analysis of the effect of the variable charging current control method on cycle life of li-ion batteries," *Energies*, vol. 12, no. 15, pp. 3023, Aug. 2019.

[23] Met Office. (2016). MIDAS: UK hourly weather observation data. NCAS British Atmospheric Data Centre. (2019, Feb. 12). [Online]. Available: https://catalogue.ceda.ac.uk/uuid/916ac4bbc46f7685ae9a5e10451bae7c.

[24] S. Frank and S. Rebennack, "An introduction to optimal power flow: theory, formulation, and examples," *IIE Transactions*, vol. 48, no. 12, pp. 1172–1197, Aug. 2016.

[25] R. D. Zimmerman, C. E. Murillo-Sánchez, and R. J. Thomas, "MATPOWER: steady-state operations, planning, and analysis tools for power systems research and education," *IEEE Transactions on Power Systems*, vol. 26, no. 1, pp. 12–19, Feb. 2011.

[26] C. Chen, H. B. Sun, X. W. Shen, Y. Guo, Q. L. Guo, and T. Xia, "Two-stage robust planning-operation co-optimization of energy hub considering precise energy storage economic model," *Applied Energy*, vol. 252, pp. 113372, Oct. 2019.

[27] M. T. Lawder, B. Suthar, P. W. C. Northrop, S. De, C. M. Hoff, O. Leitermann, M. L. Crow, S. Santhanagopalan, and V. R. Subramanian, "Battery energy storage system (BESS) and battery management system (BMS) for grid-scale applications," *Proceedings of the IEEE*, vol. 102, no. 6, pp. 1014–1030, Jun. 2014.

[28] J. Dixon, P. B. Andersen, K. Bell, and C. Træholt, "On the ease of being green: an investigation of the inconvenience of electric vehicle charging," *Applied Energy*, vol. 258, pp. 114090, Jan. 2020.

[29] R. F. Zhang, B. Z. Xia, B. H. Li, L. B. Cao, Y. Z. Lai, W. W. Zheng, H. W. Wang, W. Wang, and M. W. Wang, "A study on the open circuit voltage and state of charge characterization of high capacity lithium-ion battery under different temperature," *Energies*, vol. 11, pp. 2408, Sep. 2018.

[30] G. Carpinelli, A. R. Di Fazio, S. Khormali, and F. Mottola, "Optimal sizing of battery storage systems for industrial applications when uncertainties exist," *Energies*, vol. 7, no. 1, pp. 130–149, Jan. 2014.

[31] B. L. Xu, A. Oudalov, A. Ulbig, G. Andersson, and D. S. Kirschen, "Modeling of lithium-ion battery degradation for cell life assessment," *IEEE Transactions on Smart Grid*, vol. 9, no. 2, pp. 1131–1140, Mar. 2018.

[32] R. Ak, V. Vitelli, and E. Zio, "Uncertainty modeling in wind power generation prediction by neural networks and bootstrapping," in *Proceedings of the ESREL 2013*, Amsterdam, Netherlands, 2013, pp. 1–6.

[33] The Wind Power. V47/660 (Vestas). (2019, Feb. 12). [Online]. Available: https://www.thewindpower.net/scripts/fpdf181/turbine.php?id=176.

[34] The Wind Power. V52/850 (Vestas). (2019, Feb. 12). [Online]. Available: https://www.thewindpower.net/scripts/fpdf181/turbine.php?id=27.

[35] The Wind Power. E44/900 (Enercon). (2019, Feb. 12). [Online]. Available: https://ww.thewindpower.net/scripts/fpdf181/turbine.php?id=2.

[36] The Wind Power. E82/3000 (Enercon). (2019, Feb. 12). [Online]. Available: https://www.thewindpower.net/scripts/fpdf181/turbine.php?id=554.

[37] A. Stepek and I. L. Wijnant, "Interpolating wind speed normals from the sparse Dutch network to a high resolution grid using local roughness from land use maps," Koninklijk Nederlands Meteorologisch Instituut, De Bilt, Netherlands, Tech. Rep. TR-321, 2011.

[38] F. Fan, "Enhanced weather modelling for dynamic line rating," Ph.D. dissertation, University of Strathclyde, Glasgow, 2018.

[39] F. Fan, K. Bell, D. Hill, and D. Infield, "Wind forecasting using kriging and vector auto-regressive models for dynamic line rating studies," in *Proceedings of 2015 IEEE Eindhoven PowerTech*, Eindhoven, Netherlands, 2015, pp. 1–6.

[40] MATLAB Release 2016a, The MathWorks, Inc., Natick, MA, USA.

[41] R. D. Zimmerman and C. E. Murillo-Sánchez. (2016). MATPOWER (Version 6.0). [Online]. Available: http://matpower.org.doi:10.5281/zenodo.3237810.

Fulin Fan received the B.Eng. Degree in 2012 from both North China Electric Power University, Baoding, China, and the University of Strathclyde, Glasgow, U.K., where he received the Ph.D. degree in 2018, all in Electronic and Electrical Engineering. From 2016 to 2018, he was a Research Assistant with the University of Strathclyde, where he has been a Research Associate since 2018. His research interests include energy storage optimization, real-time thermal rating forecasting for overhead lines, and electric traction system modeling.

Ivana Kockar (S'99–M'04–SM'17) received the Dipl.-Ing. (MEng) degree from the University of Belgrade, Belgrade, Serbia, and the MSc and Ph.D. from McGill University, Montreal, Canada. She is a Reader within the Institute for Energy and Environment at the University of Strathclyde, Glasgow, U.K. Her research work is in the area of operation of power systems and electricity markets, including integration of distributed energy resources and multi-vector local energy systems and market, as well TSO-DSO coordination. Dr. Kockar is a past chair of the IEEE PES Computing and Analytical Methods Subcommittee (CAMS).

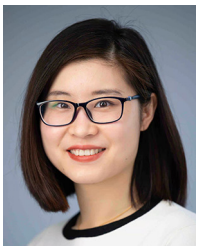

Han Xu received the B.Eng. degree from both Shanghai University of Electric Power, Shanghai, China, and the University of Strathclyde, Glasgow, U.K., in 2012, where she received the Ph.D. degree in 2020, all in Electronic and Electrical Engineering. She was a Research Assistant from 2015 to 2019 at the University of Strathclyde and is currently a R&D engineer at Power Networks Demonstration Centre, Glasgow, U.K., since 2019. Her research interests include power system analysis and modeling, demand side response, energy storage, DSO transition and commercial analysis of distribution ancillary services.

Jingsi Li received the Master degree in Land Resources Management from Wuhan University, Wuhan, China, in 2016. She is currently pursuing the Ph.D. degree in Civil and Environmental Engineering at the University of Strathclyde, Glasgow, U.K., since 2016. Her research interests include spatial interpolation, GIS applied to transport system and micro-simulation, data acquisition and analysis of travel behaviour, and land-use transport interaction.